Journal Pre-proof

Microstructural homogeneity and mechanical behavior of a selective laser melted Ti-35Nb alloy produced from an elemental powder mixture

Jincheng Wang, Yujing Liu, Chirag Dhirajlal Rabadia, Shun-Xing Liang, Timothy Barry Sercombe, Lai-Chang Zhang

Please cite this article as: Wang J, Liu Y, Rabadia CD, Liang S-Xing, Sercombe TB, Zhang L-Chang, Microstructural homogeneity and mechanical behavior of a selective laser melted Ti-35Nb alloy produced from an elemental powder mixture, *Journal of Materials Science and amp; Technology* (2020), doi: https://doi.org/10.1016/j.jmst.2020.05.052

This is a PDF file of an article that has undergone enhancements after acceptance, such as the addition of a cover page and metadata, and formatting for readability, but it is not yet the definitive version of record. This version will undergo additional copyediting, typesetting and review before it is published in its final form, but we are providing this version to give early visibility of the article. Please note that, during the production process, errors may be discovered which could affect the content, and all legal disclaimers that apply to the journal pertain.

Research Article

Microstructural homogeneity and mechanical behavior of a selective laser melted Ti-35Nb alloy produced from an elemental powder mixture

Jincheng Wang [1,2], Yujing Liu [2], Chirag Dhirajlal Rabadia [1], Shun-Xing Liang [1], Timothy Barry Sercombe [2,*], Lai-Chang Zhang [1,*]

[1] *School of Engineering, Edith Cowan University, 270 Joondalup Drive, Joondalup, Perth, WA 6027, Australia*

[2] *School of Engineering, M050, The University of Western Australia, 35 Stirling Highway, Crawley, Perth, WA 6009, Australia*

[*]Corresponding authors.

E-mail addresses: l.zhang@ecu.edu.au, lczhangimr@gmail.com (L.-C. Zhang), tim.sercombe@uwa.edu.au (T.B. Sercombe).

Abstract

Although using elemental powder mixtures may provide broad alloy selection at low cost for selective laser melting (SLM), there is still a concern on the resultant microstructural and chemical homogeneity of the produced parts. Hence, this work investigates the microstructure and mechanical properties of a SLM-produced Ti-35Nb composite (in wt%) using elemental powder. The microstructural characteristics including β phase, undissolved Nb particles and chemical homogeneity were detailed investigated. Nanoindentation revealed the presence of relatively soft undissolved Nb particles and weak interface bonding around Nb-rich regions in as-SLMed samples. Solid-solution treatment can not only improve chemical homogeneity but also enhance bonding through grain boundary strengthening, resulting in ~43% increase in tensile

1

elongation for the heat-treated Ti-35Nb compared to the as-SLMed counterpart. The analyses of tensile fractures and shear bands further confirmed the correlation between the different phases and the ductility of Ti-35Nb. In particular, the weak bonding between undissolved Nb and the matrix in the as-SLMed sample reduces its ductility while the β grains in solid-solution treated Ti-Nb alloy can induce a relatively stable plastic flow therefore better ductility. This work sheds insights into the understanding of homogenization of microstructure and phases of SLM-produced alloys from an elemental powder mixture.

Key words: Titanium-Niobium; Selective laser melting; Microstructure; Nanoindentation; Mechanical behavior

1. Introduction

Additive manufacturing (AM) has created a significant paradigm shift in a variety of industries, including aerospace[1], automotive[2, 3], and biomedical[4, 5] sectors. One of the main benefits of AM is that it drives the advancement of biomedical and manufacturing engineering through its superior ability to rapidly tailor patient-specific and complex-structured products with the minimal wastage of materials and with a shorter time to market[6, 7]. Selective laser melting (SLM)[8-11] is one of the recently developed AM technologies, where a laser beam selectively irradiates and melts the metallic powder layer-by-layer that guided from computer-aided design models[12]. SLM is an effective method for fabricating near net-shaped components using a metallic powder feedstock. In particular, the powder particle size[13], chemical composition[14, 15], scanning parameters[16-19] and post heat treatment[12, 20, 21] can all affect the microstructure and mechanical properties of SLM-produced products. However, the SLM process usually uses pre-alloyed powder as a feedstock, which is time consuming to produce, expensive and therefore available in a limited range of compositions[16]. In contrast, the use of elemental powder mixtures combined with in-situ alloying is a potential route to lower powder cost and to expand near infinite compositional possibilities[12, 22, 23].

Titanium and its alloys are known as a type of attractive and advantageous metallic biomaterials to replace dysfunctional hard tissues due to their novel biocompatibility[24, 25], satisfactory modulus-to-strength ratio[26, 27] and excellent corrosion resistance[28-30]. However, surgical implants made of metallic alloys have a higher elastic modulus compared to the adjacent natural bones, which causes the well-known stress shielding phenomenon in the bones, preventing bone remodelling and leading to bone resorption and eventually failure of the implants[31]. An

effective solution to minimize the stress shielding effect is to tailor the modulus of the material to be as close as possible to that of the bone it replaces. Recently, β-type titanium alloys have shown high potential as surgical implant materials, owing to their relatively lower modulus[32, 33]. In these alloys, the low-stiffness metastable β phase is obtained at room temperature through the addition of certain amount of β phase stabilizers, such as V, Mo, Ta and Nb[12, 34]. Of these β stabilizers, V ions in the human body can cause many neurological diseases [35], while Mo and Ta have much higher density and higher melting point than Nb[12]. Therefore, Nb is one of the most favored β phase stabilizer to form Ti alloys with a reduced elastic modulus[33, 36], with an increased shape memory recovery rate [37] and with enhanced corrosion resistance and improved biocompatibility[14]. As such, Ti-Nb alloys with a β phase microstructure and nontoxic alloying elements have been widely studied as alternative low-modulus biomaterials. These alloys include β-type Ti-45Nb (in wt%, the same hereafter)[17, 38], Ti-Nb-Zr-Sn[39-41], Ti-Nb-Zr-Mo-Sn[26] and Ti-Nb-Ta-Zr[42, 43] alloys. Additionally, in-vitro and in-vivo studies on the biocompatibility of Ti-Nb alloys revealed an improvement in tissue adhesion and proliferation [44].

By taking full advantages of the commercial availability and lower cost of elemental Ti and Nb powder, the synthesis of Ti-Nb composites has attracted recent attention[14, 45]. Traditional manufacturing methods, such as forging[46], cladding[47], pressure-less sintering[20] and spark plasma sintering[20, 46], have all been explored in manufacturing Ti-Nb alloys from powder mixtures due to their high efficiency in bulk volume production. However, they also have many limitations, such as being time-consuming, requiring cost-intensive post-processing and having high material wastage when producing complex structures [48]. In contrast, SLM can quickly manufacture complex-shaped components by selectively melting a powder mixture of different metallic materials with a high-energy laser beam[12, 22]. However, the differences between the particle size, powder density and melting temperature of the elemental powders are the main reported obstacles in the production of a homogeneous microstructure and uniform distribution of the chemical elements in the SLM process[12, 14, 16, 45, 46, 49]. In particular, a large difference in particle size can lead to powder segregation, partial melting and an unstable melt pool. This leads to variations in the density and can cause segregation and inhomogeneity[12]. Similarly, significant differences in the melting point can result in undissolved particles during the SLM process[12, 16, 45]. The melting point and density of Ti (1668 °C, 4.5 g/cm^3 respectively) are about two-thirds and half respectively of those for Nb (2468 °C, 8.6 g/cm^3 respectively). Fischer et al.[16] produced in-situ alloyed Ti-40.5Nb alloy from elemental powder mixtures using SLM and showed that while by tuning the scanning parameters, the chemical homogeneity could be maximized but a fully homogeneous structure could not be produced. Zhuravleva et al.[50] used ball-milled Ti-40Nb powder mixture in the SLM process, but

3

they could only produce a highly porous microstructure. The SLM-produced Ti-39.3Nb from an elemental powder mixture[16, 45] also displays chemical and microstructural inhomogeneity despite the retained fully metastable β phase with excellent biocompatibility. In addition, the effect of Nb concentration, the powder feedstock type and manufacturing method have been widely explored to study the microstructure and mechanical properties of Ti-Nb powder mixture[14, 16, 17, 45, 50-52]. Note that, the resultant SLM-produced Ti-Nb alloys demonstrate a range of microstructure and mechanical properties. Those researches have presented many novel findings in terms of improving synthesized Ti-Nb alloys from an elemental powder mixture even though there are still unresolved issues such as how to ensure chemical and microstructural homogeneity. Our previous work on SLM-produced Ti-35Nb alloy[12] investigated a feasible approach to manufacture a β-type Ti-Nb composite with low Young's modulus and high strength from elemental powder mixture. Our results indicate that the resultant heterogeneous microstructure has an adverse effect on the compressive deformation behavior and corrosion performance. However, detailed investigations of homogeneity and corresponding phase effect on the parts produced through SLM using an elemental Ti-Nb powder mixture are limited. The studies on the effects of microstructural homogeneity, undissolved Nb particles and annealing on the mechanical properties and deformation behaviors can enhance the understanding of SLM-produced Ti-Nb composites from an elemental powder mixture.

In addition, Hon et al.[53] investigated the effect of Nb-content (from 14 wt% to 40 wt%) on the microstructure of hot-rolled Ti-Nb alloys and indicated that a fully β phase is achieved at room temperature when the concentration of Nb exceeds 34 wt%. Moreover, it has been reported that the Nb-content above 35 wt% in binary Ti-Nb alloy has promising shape memory effect[54, 55]. However, Yılmaz et al.[14] revealed an increased porosity and chemical inhomogeneity using mixed Ti-Nb powder with increasing the Nb content from 27 wt% to 56.4 wt%. As such, in this work, Ti-35Nb composites were manufactured from an elemental mixed powder consisting of 65 wt% Ti and 35 wt% Nb. These powders had an almost identical particle size. The microstructure and grain morphology were investigated before and after heat treatment. In addition, the reduced elastic modulus and nano-hardness were measured in order to interpret the intrinsic properties of constituent phases and to determine microstructural heterogeneity. Mechanical properties (strength, elongation, hardness and elastic modulus) were also evaluated.

2. Experimental methods

2.1. Materials preparation

4

The commercially pure titanium powder (CP-Ti, particle size 40 - 65 μm, ASTM Grade 2, TLS Technik, Germany) with chemical composition 0.14Fe, 0.142O, 0.01C, 0.007N, 0.001H and Ti balance (wt%) and the niobium powder (Nb, particle size 40 - 65 μm, Sophia's Wholesale, China, chemical composition 0.04Fe, 0.02Al, 0.32O, 0.05C, 0.005N, 0.032H and Nb balance (wt%)) were used in this work. A mixture of 65 wt% Ti and 35 wt% Nb elemental powder was mixed for 1 h using a Turbula T2F mixer. A Mastersizer 2000 (Malvern, UK) was used to analyze the powder particle size distribution. Fig. 1 shows the particle size, morphology and chemical composition of powder mixture. The distribution curves of the CP-Ti, Nb, and Ti-35Nb mixed powder (Fig. 1(a)) show that although the two elemental powder had close average particle size (d_{50}) (as shown the table in Fig. 1(a) inset), the Nb powder had a wider particle size distribution. As shown from the morphology of mixed powder (Fig. 1(b)), the CP-Ti powder was spherical in morphology while the Nb particles were irregular and contained many satellites (Fig. 1(b)). The measured chemical composition of the Ti-35Nb mixed powder using EDS (Fig. 1(c)) was 65.6 wt% Ti and 34.4 wt% Nb.

2.2. Sample preparation and heat treatment

Cylindrical specimens with dimensions of 9 mm in diameter and 60 mm in length were made using a Realizer SLM-100 SLM machine (200 W, 40 μm spot size, 1.064 μm wavelength fibre laser (Yb:YAG), Germany). The oxygen content in build chamber was managed at below 0.1% using high purity Ar gas to minimize oxidation[56]. The substrate preheating temperature was 200 °C and the scanning strategy used rotated the scanning vectors 90° between layers. The SLM processing parameters used in this work are listed in Table 1. The resultant volumetric energy density, E, (in J/mm^3) was then computed using Eq. (1)[57]:

$$E = \frac{P}{v \cdot s \cdot t}$$ (1)

where P is the laser power (W), v is the laser scanning speed (mm/s), s is the hatch space (mm) and t is the layer thickness (mm). The E is a specified value that can be used to quantify the SLM processing parameters to measure the total amount of incident laser energy that is focused onto the powder bed. This energy causes the melting and can enhance diffusion of metallic powder in the SLM process. The layer thickness and hatch spacing for Ti-Nb alloys were 50 μm and 100 μm, respectively[58, 59]. As the laser scanning speed decreases, the laser-powder interaction time increases, which can leads to an increase in the laser energy density and melt pool size[60, 61]. However, excessive energy (at very low scanning speed) can lead to highly dynamic melt pool (i.e. Marangoni convection), which can result in the distortion of melt tracks and increase of porosity[41,

5

[62]. At high laser scan speeds, there is insufficient energy to completely melt the powder and significant porosity results. As such, the scanning speeds were varied from 500 mm/s to 1250 mm/s in this work. The theoretical density of Ti-35Nb was 5.43 g/cm^3. The relative density measured using Archimedes principal (Table 1) indicates that a relatively high density (99.0 ± 0.4%) at energy density of 80 J/mm^3 could be obtained. Therefore, the samples produced at this energy density were used for further work.

It has been reported that microstructural and chemical inhomogeneity occurred in the SLM-produced Ti-Nb alloy using an elemental powder mixture is attributed to the presence of undissolved Nb[14, 16]. Post heat treatment of SLM-produced alloys can improve the microstructural and chemical homogeneity. Since the diffusion of Nb into Ti is both time (5–24 h) and temperature (800–1300 °C)[12, 63-65] dependent, a post heat treatment (24 h, 1000 °C)[12, 65] was adopted in this work. The post heat treatment was controlled in a tube furnace under an Argon flow rate of 0.5 L/min. Cylindrical specimens were annealed at 5 °C/min to 1000 °C, held for 24 h and then removed from the furnace and air cooled.

2.3. Mechanical testing

According to the ASTM E8 standard, the specimens for tensile testing with gauge diameter of 4 mm and length of 16 mm were machined from as-SLMed and heat-treated samples along the build plane (i.e., the XY-plane). All the tensile tests were performed at a strain rate of 0.5 mm/min on Instron 5982 universal machine (with the load cell capacity of 100 kN). The tensile yield strength (using 0.2% strain offset method as per the ASTM E111), ultimate tensile strength and elongation were determined from the engineering stress-strain curves. The tensile test results reported in this work were averaged from 3 individual experiments for each condition. Young's modulus measurement was performed according to the ASTM E1876-15 using a RFDA basic (IMCE NV, Belgium) at room temperature. The as-built samples were machined down to 8 mm diameter and 3 samples were tested for each condition. As nanoindentation test can evaluate the elastic modulus and hardness of material at the nanometer scale[66], it was employed to study the characteristics (e.g. bonding, homogeneity) of the interfaces and constituent phases in the matrix. Nano-modulus/hardness mapping (with an area of 150 μm × 150 μm) was performed on the build plane (cross-sections of XY-plane) using a Hysitron Triboindenter, which was equipped with a Berkovich diamond indenter with a tip radius of 100 nm. A total of 225 indents (in a matrix of 15 × 15) were performed and the space between each indent was 10 μm. The applied maximum indentation force was kept constant at 5 mN and the loading and unloading rate was 200 μN/s, based on the standard trapezoid load function. The Vickers micro-hardness tests were carried out on

6

a polished surface with a load of 10 kgf and a dwell time of 20 s. The Vickers hardness was measured in at least 10 random positions.

2.4. Characterizations

The phase constituents of the specimens were characterized by X-ray diffraction (XRD, PANalytical Empyrean, Netherlands) with Cu-Kα radiation (wavelength λ=0.15406 nm) at 40 kV and 40 mA. The scanning rate was 0.06 °/s and scanning angle (2θ) was in the range of 30° to 80°. Samples for microstructure characterization were ground by using silicon carbide papers up to 2000 grits. The ground samples were then ultrasonically cleaned in distilled water for 10 min, and sequentially polished with standard metallographic techniques using MD-Mol and MD-Chem polishing clothes. The microstructure and fracture surface were characterized at 20 kV and 1.6 nA by scanning electron microscopy (SEM, FEI Verios XHR 460) attached with energy dispersive spectroscopy (EDS, Aztec)[9]. X-ray micro-computed tomography (Micro-CT, Zeiss Versa 500) was performed at voltage of 140 kV and power of 10 W with a voxel size of 3.76 μm, which enabled the device detector to detect the undissolved Nb particles with equivalent diameters above 5 μm. Each of the 3200 projections had an exposure time of 2 s. Three individual samples were scanned before and after heat treatment. The collected Micro-CT raw data were then processed by Avizo 8.1 software to determine the undissolved Nb distribution and to measure the undissolved Nb volume fraction in a cubic volume of interested of 3.4 mm^3. A non-local means filter was used to smooth the data and remove noise, then an automatic thresholding was employed on a grayscale image via the factorisation method and Otsu criterion[67]. These parameters were kept constant for analysis of each individual sample.

3. Results and discussion

3.1. Microstructural features

Fig. 2 illustrates the XRD patterns of the Ti-35Nb powder mixture together with elemental CP-Ti and Nb powder. The CP-Ti only possesses the hexagonal close-packed (hcp) α phase and the Nb powder comprises just the body-centered cubic (bcc) Nb phase. The phases of the Ti-35Nb mixed powder correspond to the respective peaks of CP-Ti and Nb, indicating no phase transformation has occurred during powder mixing process. Fig. 2 also displays the XRD patterns of the SLM-processed and heat-treated Ti-35Nb samples, indicating both samples are composed of the metastable bcc β phase, trace quantities of α/α'' phases, and undissolved Nb. In addition, the peak of 2θ may correspond to bcc Nb or β phase due to very close lattice parameters of Nb to that of Ti-Nb β phase, which makes it hard to distinguish these two phases on the XRD patterns. It can be seen

7

that the peak at about $2\theta = 70°$ is slightly broader in the as-SLMed alloy than in the Nb powder and powder mixture. Therefore, it is likely that this peak corresponds to both Nb and β phase, which agrees well with the literature[16]. Sufficiently high laser energy can fully melt the CP-Ti powder (melting temperature 1668 °C) in the melt pool. Upon cooling, the melt pool initially solidifies to form the β phase and then transformation of the β phase to α phase takes place below the allotropic transformation (~882.5 °C)[68]. In order to obtain β phase at room temperature, β phase stabilizers (e.g. Nb) need to diffuse into Ti to avoid the martensitic transformations (such as β→ω, β→α, β→α' and β→α") during cooling[42]. The addition of sufficient β stabilizers can lower the β to α martensitic start temperature to below room temperature, resulting in the β phase being retained down to room temperature. The Molybdenum equivalent (Mo_{eq}) is an empirical parameter that indicates the β phase stability for a given alloy. The effect of combination of β stabilizing elements can be predicted against a single amount of Mo (β stabilizer) required[22]. In general, a fully β phase can be retained during quenching with Mo_{eq} with value of approximately 10% and the β phase stability increases with an increased Mo_{eq} value[34]. The Mo_{eq} value of an alloy with given alloying elements can be calculated by Eq. (2)[12, 34]:

$$Mo_{eq} = 1.0Mo + 0.67V + 0.44W + 0.28Nb + 0.22Ta + 2.9Fe + 1.6Cr + 1.54Mn + 1.7Co + 1.25Ni - 1.0Al \ [wt.\%] \tag{2}$$

Using Eq. (2), the Mo_{eq} of Ti-35Nb alloy is 9.8%, which is very close to the concentration required to fully stabilize the β phase (~10%). In addition, it has been reported after quenching a low content of β phase stabilizer can lead to the formation of α or α' phase, while a relatively high concentration may transform β phase to orthorhombic martensite α"[42,54, 69-71]. Moreover, increasing the cooling rate can facilitate α" martensitic phase transformation from β phase for Ti-Nb alloys[71]. The XRD results (Fig. 2) confirm the relatively high concentration of β stabilizer (35 wt% Nb), which together with the rapid cooling rate of the SLM process result in the formation of metastable β phase and trace amounts of martensite α" phase.

Fig. 3(a) is a SEM image of the as-SLMed Ti-35Nb sample, which displays an inhomogeneous microstructure. Undissolved Nb particles (light colored) are randomly distributed in the matrix. The high melting temperature of Nb (2468 °C) has resulted in incomplete melting of the particles, which combined with the short laser interaction time and rapid melt pool cooling (10^5–10^8 K/s)[8] have resulted in limited interdiffusion of the elements. The net result is both partially unmelted Nb particles and a very inhomogeneous composition, as shown by the EDS maps of Fig. 3(b) and (c). Such lack of homogeneity is likely to result in undesirable chemical or mechanical properties. Fig.

3(d) is the EDS result from the point d as indicated on Fig. 3(a). At this point, the chemical composition is 60.5 wt% Ti and 39.5 wt% Nb, which is close to the nominal composition (with 65 wt% Ti and 35 wt% Nb). This suggests that in some areas, chemical homogeneity can be approximately achieved during the SLM process.

3.2. Surface morphology and homogeneity

Fig. 4(a) shows the micro-CT image (3D imaging) of the as-SLMed Ti-35Nb. The light-colored undissolved Nb particles are randomly distributed throughout the material. After homogenization treatment, a significant reduction in the amount of Nb particles is evident as shown in Fig. 4(b). The reconstructed quantitative micro-CT images of as-SLMed and heat-treated Ti-35Nb are illustrated in Fig. 4(c) and (d), respectively. It is apparent that the morphology and distribution of Nb particles in the reconstructed images are nearly identical with original micro-CT images. From the reconstructed micro-CT images, the volume fraction of undissolved Nb in the as-SLMed and heat-treated Ti-35Nb was determined to be 3.8±0.5% and 1.3±0.3%, respectively. However, the voxel size (resolution) of the micro-CT is 3.76 μm, and therefore only unmelted Nb larger than ~5 μm in size would be detected. As such, it is possible that not all the undissolved Nb particles have been detected, making it likely that these fraction are an underestimation. In Fig. 4(e) and (f), only the undissolved Nb are shown for the as-SLMed and heat-treated Ti-35Nb samples. It is clear that the undissolved Nb particles (in irregular shape) are randomly distributed throughout the samples and that heat treatment has resulted in a significant reduction in the number of Nb particles as a result of diffusion of Nb into the matrix.

The backscattered SEM images of as-SLMed Ti-35Nb in Fig. 5(a) and (b) show a dendritic microstructure containing undissolved Nb particles of different sizes which are randomly distributed in the Ti-Nb matrix. The matrix itself also has a variable composition, as shown by the EDS line analysis in Fig. 5(e). These results suggest that the short laser-powder interaction time and the very rapid cooling of the molten pool lead to insufficient time for the complete dissolution and diffusional redistribution of the Nb. As such, distinct segregation occurs. The dendritic grains (Fig. 5(b) inset) are formed as a result of high thermal gradient, fast cooling, and moderate solidification rate of the material during the SLM process[12,59]. It has been reported that a moderate ratio of temperature gradient to solidification rate (G/R ratio) can induce a columnar or cellular dendritic microstructure[12]. Both the Ti and Nb possess a relatively high thermal conductivity (21.9 W/mK and 54 W/mK respectively)[12], which results in a fast heat dissipation (very high thermal gradient G) in Ti-Nb molten pool and substrate. The rapid cooling (10^5–10^8 K/s)[8] leads to a short solidification time (moderate solidification rate R). Therefore, the moderate G/R ratio and high solute Nb content

(heterogeneous nucleation sites) in the molten pool[45] lead to form dendritic grains in the SLM-produced Ti-35Nb.

The metastable β titanium alloys can be tailored to produce specific microstructures in the course of annealing[34,72]. As the mechanical and chemical properties largely rely on microstructure, grain size and morphology[39,70], the SLM-produced Ti-35Nb sample made from elemental mixed powder can be annealed to improve its microstructural and chemical homogeneity. After homogenization treatment (1000 °C, 24 h), the microstructure (Fig. 5(c)) shows that significant β grain growth has occurred (Fig. 5(d)) and undissolved Nb particles still exist (although with reduced grain size). This is consistent with the micro CT results shown in Fig. 4. Nonetheless, it is clear that there is much more uniform distribution of Ti and Nb in Fig. 5(f), indicating significantly improved microstructural homogeneity. It is expected that these different microstructures would result in different mechanical properties and fracture behaviors.

It is known that nanoindentation can be employed as a non-destructive method to examine the local mechanical properties of various materials and has advantages for in-situ measuring capability without affecting the microstructure[66,73]. From the contour maps of reduced elastic modulus and nano-hardness in Fig. 6, one can directly interpret the intrinsic properties of the constituent phases and microstructural heterogeneity. The measured value of reduced elastic modulus (E_r) for the bulk material can be obtained using the Oliver and Pharr method from the nanoindentation test. Then, the value of E_r can be used to calculate the elastic modulus (E) using Eq. (3)[73]:

$$E = \frac{(1-v^2)E_r E_i}{E_i - E_r(1-v_i^2)} \tag{3}$$

where v is Poisson's ratio of test material, E_i and v_i are elastic modulus and Poisson's ratio of indenter material, respectively. For the diamond indenter used in this work, $E_i = 1141$ GPa and $v_i = 0.07$[73].

Fig. 6 shows the results of the large-scale nanoindentation mapping on the as-SLMed Ti-35Nb material and heat-treated counterpart. A large number of indents (225 indents) were performed (as shown in Figs. 6(a) and (b)) to produce the contour plots of Fig. 6(c)-(f). The large variation in the reduced elastic modulus (E_r) contour map of Fig. 6(c) is attributed to the phase variation and chemical inhomogeneity of the as-SLMed Ti-35Nb. Those contours with irregular boundaries indicate the non-uniform distribution of undissolved Nb particles, Nb segregation zones and Ti-Nb β phase in the microstructure, which is consistent with microstructural observations of Fig. 6(a). For the as-SLMed Ti-35Nb sample, the undissolved Nb particles and Nb-rich zones (solid contour line

in Fig. 6(c)) exhibit a much higher E_r (109±7 GPa) than the surrounding inhomogeneous Ti-Nb β phase (88 ± 5 GPa). After heat treatment, the variation in E_r has been substantially reduced (Fig. 6(d)) and the structure is dominated by a more uniform Ti-Nb phase with E_r of 91 ± 6 GPa.

The nano-hardness mapping of as-SLM Ti-35Nb (Fig. 6(e)) reveals substantially large fluctuations in hardness (1.80–5.68 GPa), which is a result of the presence of softer undissolved Nb areas (solid contour line in Fig. 6(e)) embedded in the stronger Ti-Nb β phase (4.23–5.68 GPa). Similar to the reduced elastic modulus, the homogenization heat treatment has significantly reduced the hardness variability (Fig. 6(f)), which now ranges from 3.26 to 5.20 GPa (and mostly from 4.23 to 5.20 GPa). The large and regular contours (yellow and orange areas) indicate the Ti-Nb phases under different grain boundaries. It signifies that the heat-treated Ti-35Nb sample has improved uniformity of the hardness distribution, agreeing well with the microstructural analysis in Fig. 5(d) and (f). Consequently, the nanoindentation mappings reveal essential microstructural features (phase distribution) and evidence of different phase responses (nano-hardness).

3.3. Patterns of nanoindentation and Vickers indentation

In order to fully understand the effect of the inhomogeneous microstructure and undissolved Nb particles on the SLM-produced Ti-35Nb, nanoindentation load-displacement curves have been reproduced in Fig. 7. The load-displacement curves in Fig. 7(a) show significantly different responses after indentation in each of the phases. The Ti-Nb β phase has the smallest penetration depth (displacement after unloading), followed by the interface. The undissolved Nb phase in the as-SLMed Ti-35Nb has the largest penetration depth, indicating a low hardness of the undissolved Nb (large deformation in inset image). Therefore, it is clear that there exists a significant spatial variation in properties as a result of the inhomogeneous microstructure. In contrast to the as-SLMed alloy, Fig. 7(b) shows smooth load-displacement curves that are essentially identical for the 6 different positions indicated on the inset SEM image. The indents are also almost identical in size. This further confirms the improved homogeneity of the Ti-Nb phase microstructure after heat treatment.

It is known that the macroscopic elasto-plastic behavior of a metallic material can be analyzed from the formation of localized plastic deformation patterns surrounding micro-hardness indents[74, 75]. After testing, the formation of slip bands (straight lines or wavy lines) around indenters under the strain localization indicates plastic deformation in the area. Straight slip bands (regular parallel lines) are normally distributed along the edges of the indentation. In contrast, wavy slip bands (rough semicircular or irregular lines) are usually initiated near indenter edges and are distributed at

11

the indentation corner. The ability of a material to plastic deformation is directly proportional to the size of the deformation zone comprising slip bands around the indentation edges and corners[76]. Generally, the formation of straight slip bands denotes that a material undergoes less plastic deformation compared to one that forms wave-like slip bands[12,76]. Fig. 8 shows the indent pattern (backscattered SEM images) and the slip bands that have formed around the hardness indents of as-SLMed and heat-treated Ti-35Nb samples. Fig. 8(a) and (b) show that a large deformation zone comprising accumulated straight slip bands has formed around the indentation edges. These straight slip bands have formed as a result of the normal stress components[77]. The accumulation of slip bands in the as-SLMed Ti-35Nb are caused by the plastic incompatibility between the different constituent phases (Fig. 7(a)). For the heat-treated Ti-35Nb material (Fig. 8(c) and (d)), straight and wavy slip bands surround all 4 corners and edges of the indenter as a result of both the normal and shear stress components. The slip bands either stop or change the direction at grain boundaries due to a different crystallographic orientation of each grain. The significantly reduced and homogeneously distributed slip bands suggest an enhanced microstructural homogeneity in the SLM-produced Ti-35Nb after heat treatment.

3.4. Mechanical properties

Fig. 9 displays the tensile stress-strain curves of the Ti-35Nb samples. Despite microstructural and chemical inhomogeneity, the as-SLMed Ti-35Nb possesses relatively high tensile strength. The Fig. 9 inset shows that brittle fracture has occurred in the as-SLMed sample. These results indicate that the formation of fine dendritic grains (Fig. 5(b)) efficiently impede dislocations, thereby enhancing strength but limiting ductility. The heat-treated Ti-35Nb counterpart has an enhanced tensile ductility, despite of slightly lower tensile yield strength compared to that of the as-SLMed Ti-35Nb. The lower yield strength most likely results from grain growth (Fig. 5(d), which results in fewer boundaries to resist dislocation motion between adjacent grains. The improved microstructural homogeneity of the heat-treated Ti-35Nb enhances grain boundary bonding of the Ti-Nb matrix and increases ductility[12].

Table 2 lists the tensile mechanical properties and Vickers hardness of the as-SLMed Ti-35Nb and its heat-treated counterpart. The heat-treated Ti-35Nb samples shows higher Vickers hardness (311±16 HV) than the as-SLMed counterparts (274±7 HV); both Ti-35Nb samples exhibit much larger hardness than as-SLMed CP-Ti (213±11 HV)[68], as-SLMed Ti-40.5Nb powder mixture (266±5 HV)[16] and the prealloyed, low modulus β-type Ti-24Nb-4Zr-8Sn (220±6 HV)[41] as well as the Ti-25Nb-3Zr-3Mo-2Sn (202-230 HV)[26]. The relative low hardness of as-SLMed sample is attributed to the presence of large undissolved Nb particles, which exhibit very low hardness (Figs.

12

6(e) and 7(a)). The heat treatment process, which creates a more homogeneous Ti-Nb β phase, enhances the hardness of the material through enhanced solid solution hardening[12,14,45,49]. The yield strength of as-SLMed (648±13 MPa) and heat-treated Ti-35Nb (602±14 MPa) are significantly greater than that of the as-SLMed prealloyed Ti-24Nb-4Zr-8Sn (563±38 MPa)[41] and Ti-25Nb-3Zr-3Mo-2Sn (592 ± 21 MPa)[26] as well as the as-SLMed ball milled Ti-25.5Nb (501±30 MPa), Ti-39.3Nb (516 ± 58 MPa)[45] and sintered Ti-25Nb-22Al (353–586 MPa) powder mixture[78]. But all these SLM-produced Ti alloys exhibit lower yield strength than SLM-produced pre-alloyed Ti-14Nb-13Zr alloy (794±15 MPa)[79]. In addition, these results indicate that the yield strength and hardness are not directly proportional, most likely a result of the inhomogeneous and undissolved Nb. The elastic modulus of Ti-35Nb (84±2 GPa) is approximately 25% lower than that of CP-Ti (112±3 GPa) (Table 2). The yield strength of the SLM-fabricated Ti-35Nb composite (648±13 MPa) is very close to that of CP-Ti (620±20 MPa). This result indicates that the Ti-Nb has a significantly higher strength to stiffness ratio, indicating high permissible elastic strain and better performance in surgical implant applications. Moreover, heat-treated Ti-35Nb samples exhibit a nearly 43% increase in tensile elongation compared to the as-SLMed counterpart. According to Table 2, there is also no reported deformation behavior and mechanism regarding the effect of homogeneity.

3.5. Tensile fracture

The β-type Ti-Nb alloys have been reported to have many promising properties for biomedical applications, such as excellent biocompatibility, good fracture toughness[45] and high corrosion resistance[14], along with low elastic modulus and high strength[33]. However, for any newly developed material, it is essential to investigate the tensile fracture behavior of Ti-Nb composites produced by SLM in order to understand the deformation failure mechanism, thereby reducing the chance of implant failure. Fig. 10 displays backscattered electron SEM images of the polished surface in the region of the fracture for the SLM-produced Ti-35Nb before and after heat treatment. Shear bands (deformation bands) are not observed near the fracture surface of the as-SLMed Ti-35Nb sample in Fig. 10(a), suggesting low plastic deformation and brittle fracture. The Fig. 10(a) inset shows the crack propagation around the undissolved large Nb particles. It is apparent that the weak Nb-rich regions cause failure before the material undergoes shear deformation (i.e. before the formation of shear bands). In contrast, the heat-treated counterpart (Fig. 10(b)) exhibits a large amount of shear bands, indicating that a large amount of plastic deformation has occurred after macroscopic yielding. Therefore, the heat-treated Ti-35Nb has increased elongation compared to the as-SLMed counterpart (Table 2). Additionally, multiple shear bands occur in different directions in each grain since dislocation motion is dependent on the crystallographic orientation of individual

13

grain and the amount of active slip systems[80]. It appears that cracks are initiated along grain boundaries, resulting in intergranular fracture.

Fig. 11 shows the outer edge (side view) surface fractures for Ti-35Nb samples. Fig. 11(a)-(c) reveals the dominant crack fracture (typical cleavage facet) with many fine dimples for the as-SLMed Ti-35Nb sample. The cracks are initiated around undissolved Nb particles due to the plastic mismatch between the Ti-Nb matrix and Nb-rich zone (Fig. 7(a)). This means that the Nb-rich interface may have a low resistance to dislocation motion and cracks can easily propagate under high tensile stress. The secondary fracture occurs in an intergranular mode (with fine dimples) because of the large plasticity of β phase in the matrix. Fig. 11(d)-(f) shows the intergranular fracture for the heat-treated Ti-35Nb counterpart, where the fracture path along the grain boundaries are clearly evident. The shallow dimples are homogeneously distributed on the fracture tips (Fig. 11(e)) and grain surfaces (Fig. 11(f)). The heat-treated sample has larger β grain size (Fig. 5(d)), inducing relatively stable plastic flow and better ductility.

The SEM fracture morphologies of Ti-35Nb are shown in Fig. 12. It is evident that the tensile fracture surface shows transgranular fracture, steps, and dimples for the as-SLMed Ti-35Nb sample (Fig. 12(a)-(c)). The mixed fracture is caused by the highly inhomogeneous microstructure and chemical inhomogeneity. The slips and steps form in the β phase, indicating a high strain-bearing ability of that region. After heat treatment, fracture surface (Fig. 12(d)-(f)) shows decohesion and cracks have formed along grain boundaries. This indicates that the strengthening effect of the homogeneous Ti-Nb phase has been improved as a result of strong interfacial bonding during heat treatment. The grain boundaries become a high stress concentration zone, thereby resulting in a relatively high plasticity toughness of the heat-treated material[12]. It also reveals that the improved homogeneous Ti-Nb β phase, which possesses better ductility as compared to Nb-rich phase and is beneficial to the biomedical applications of the Ti-Nb composite. Consequently, the heat treatment can improve chemical and microstructural homogeneity of SLM-produced Ti-Nb powder mixture, which could enhance the mechanical performance of Ti-Nb composites.

4. Conclusions

In this work, selective laser melting (SLM) has been used to manufacture a β-type Ti-35Nb (wt%) composite from an elemental powder mixture. The microstructure, phase response and mechanical properties of the SLM-fabricated Ti-35Nb and its heat-treated counterpart have been evaluated using a range of characterization techniques. The results provide significant advances in the understanding of the role of undissolved Nb particles, Nb-rich interfaces and Ti-Nb based β

14

phases on the mechanical performance. From this work, the following main conclusions can be drawn.

(1) The undissolved Nb particles induce microstructural inhomogeneity, which deteriorates the macroscopic plastic deformability of the as-SLMed sample. Heat treatment can achieve improved homogeneity in both microstructure and chemical composition. This enhances the mechanical properties due to the improved mechanical stability of the Ti-Nb β phase.

(2) The micro-CT 3D imaging quantification clearly illustrates that significant diffusion driven dissolution of the Nb particles occurs during the annealing treatment. The nanoindentation mappings provide direct evidence of the contribution of the different phase responses to overall mechanical properties. The Nb particle segregation zones have lower hardness and higher deformation compared to the Ti-Nb matrix. The results are consistent with the micro-hardness values.

(3) The as-SLMed Ti-35Nb exhibits relatively high tensile yield strength (648±13 MPa) due to the formation of dendritic β grains. However, the ductility is relatively low (3.9±1.1%) as a result of the weak bonding of undissolved Nb particles within the matrix. The heat-treated counterpart shows a slightly lower yield strength (602±14 MPa) but a nearly 43% increase in ductility (5.6±1.9 %) due to the improved homogeneous Ti-Nb β phase.

Declarations of Interest

The authors declare no conflicts of interest.

Acknowledgement

References

[1] D. Gu, Q. Shi, K. Lin, L. Xi, Addit. Manuf. 22 (2018) 265-278.

[2] E. MacDonald, R. Wicker, Science 353 (2016) aaf2093.

[3] J. Gao, J. Nutter, X. Liu, D. Guan, Y. Huang, D. Dye, W.M. Rainforth, Sci. Rep. 8 (2018) 7512.

[4] M. Colaco, D.A. Igel, A. Atala, Nat. Rev. Urol. 15 (2018) 213-221.

[5] L.-C. Zhang, Y. Liu, S. Li, Y. Hao, Adv. Eng. Mater. 20 (2018) 1700842 .

[6] P. Barriobero-Vila, J. Gussone, A. Stark, N. Schell, J. Haubrich, G. Requena, Nat. Commun. 9 (2018) 3426.

[7] J.H. Martin, B.D. Yahata, J.M. Hundley, J.A. Mayer, T.A. Schaedler, T.M. Pollock, Nature 549 (2017) 365-369.

[8] Y.J. Liu, Z. Liu, Y. Jiang, G.W. Wang, Y. Yang, L.C. Zhang, J. Alloys Compd. 735 (2018) 1414-1421.

[9] Y.J. Liu, S.J. Li, L.C. Zhang, Y.L. Hao, T.B. Sercombe, Scr. Mater. 153 (2018) 99-103.

[10] S.-X. Liang, X. Wang, W. Zhang, Y.-J. Liu, W. Wang, L.-C. Zhang, Appl. Mater. Today 19 (2020) 100543.

[11] Y.J. Liu, D.C. Ren, S.J. Li, H. Wang, L.C. Zhang, T.B. Sercombe, Addit. Manuf. 32 (2020) 101060.

[12] J.C. Wang, Y.J. Liu, P. Qin, S.X. Liang, T.B. Sercombe, L.C. Zhang, Mater. Sci. Eng. A 760 (2019) 214-224.

[13] J.H. Martin, B.D. Yahata, J.M. Hundley, J.A. Mayer, T.A. Schaedler, T.M. Pollock, Nature 549 (2017) 365-369.

[14] E. Yılmaz, A. Gökçe, F. Findik, H. Gulsoy, J. Alloys Compd. 746 (2018) 301-313.

[15] H. Zhang, D. Gu, J. Yang, D. Dai, T. Zhao, C. Hong, A. Gasser, R. Poprawe, Addit. Manuf. 23 (2018) 1-12.

[16] M. Fischer, D. Joguet, G. Robin, L. Peltier, P. Laheurte, Mater. Sci. Eng. C 62 (2016) 852-859.

[17] H. Schwab, K.G. Prashanth, L. Lober, U. Kuhn, J. Eckert, Metals 5 (2015) 686-694.

[18] D. Gu, X. Rao, D. Dai, C. Ma, L. Xi, K. Lin, Addit. Manuf. 29 (2019) 100801.

[19] J. Zhang, B. Song, Q. Wei, D. Bourell, Y. Shi, J. Mater. Sci. Technol. 35 (2019) 270-284.

[20] R. Karre, B.K. Kodli, A. Rajendran, N. J, D.K. Pattanayak, K. Ameyama, S.R. Dey, Mater. Sci. Eng. C 94 (2019) 619-627.

[21] S.B. Sun, L.J. Zheng, J.H. Liu, H. Zhang, J. Mater. Sci. Technol. 33 (2017) 389-396.

[22] B. Vrancken, L. Thijs, J.P. Kruth, J. Van Humbeeck, Acta Mater. 68 (2014) 150-158.

[23] H. Attar, M. Bönisch, M. Calin, L.-C. Zhang, S. Scudino, J. Eckert, Acta Mater. 76 (2014) 13-22.

[24] S. Bose, D. Ke, H. Sahasrabudhe, A. Bandyopadhyay, Prog. Mater Sci. 93 (2018) 45-111.

[25] L.-C. Zhang, L.-Y. Chen, L. Wang, Adv. Eng. Mater. 22 (2020) 1901258.

[26] Y.J. Liu, Y.S. Zhang, L.C. Zhang, Materialia 6 (2019) 100299.

[27] Y. Liu, S. Li, W. Hou, S. Wang, Y. Hao, R. Yang, T.B. Sercombe, L.-C. Zhang, J. Mater. Sci. Technol. 32 (2016) 505-508.

[28] P. Qin, Y. Liu, T. Sercombe, Y. Li, C. Zhang, C. Cao, H. Sun, L.-C. Zhang, ACS Biomater. Sci. Eng. 4 (2018) 2633-2642.

[29] L.-C. Zhang, L.-Y. Chen, Adv. Eng. Mater. 21 (2019) 1801215.

[30] P. Qin, Y. Chen, Y.-J. Liu, J. Zhang, L.-Y. Chen, Y. Li, X. Zhang, C. Cao, H. Sun, L.-C. Zhang, ACS Biomater. Sci. Eng. 5 (2019) 1141–1149.

[31] M. Niinomi, Mater. Sci. Eng. A 243 (1998) 231-236.

[32] H.J. Rack, J.I. Qazi, Mater. Sci. Eng. C 26 (2006) 1269-1277.

[33] W. Weng, A. Biesiekierski, Y. Li, C. Wen, Materialia 6 (2019) 100323.

[34] D. Doraiswamy, S. Ankem, Acta Mater. 51 (2003) 1607-1619.

[35] S. Nag, R. Banerjee, H.L. Fraser, Mater. Sci. Eng. C 25 (2005) 357-362.

[36] H.Y. Kim, Y. Ikehara, J.I. Kim, H. Hosoda, S. Miyazaki, Acta Mater. 54 (2006) 2419-2429.

[37] S. Liu, J. Liu, L. Wang, R.L.-W. Ma, Y. Zhong, W. Lu, L.-C. Zhang, Scr. Mater. 181 (2020) 121-126.

[38] Y.P. Sharkeev, V.A. Skripnyak, V.P. Vavilov, E.V. Legostaeva, A.A. Kozulin, A.O. Chulkov, A.Y. Eroshenko, O.A. Belyavskaya, V.V. Skripnyak, I.A. Glukhov, Russ. Phys. J. 61 (2019) 1718-1725.

[39] S.J. Li, T.C. Cui, Y.L. Hao, R. Yang, Acta Biomater. 4 (2008) 305-317.

[40] Y.J. Liu, H.L. Wang, S.J. Li, S.G. Wang, W.J. Wang, W.T. Hou, Y.L. Hao, R. Yang, L.C. Zhang, Acta Mater. 126 (2017) 58-66.

[41] L.C. Zhang, D. Klemm, J. Eckert, Y.L. Hao, T.B. Sercombe, Scr. Mater. 65 (2011) 21-24.

[42] M.J. Lai, T. Li, D. Raabe, Acta Mater. 151 (2018) 67-77.

[43] N. Hafeez, J. Liu, L. Wang, D. Wei, Y. Tang, W. Lu, L.-C. Zhang, Addit. Manuf. 34 (2020) 101264.

[44] J.P. Bray, A. Kersley, W. Downing, K.R. Crosse, A.J. Worth, A.K. House, G. Yates, A.R. Coomer, I.W.M. Brown, JAVMA-J. Am. Vet. Med. Assoc. 251 (2017) 566-579.

[45] Q. Wang, C.J. Han, T. Choma, Q.S. Wei, C.Z. Yan, B. Song, Y.S. Shi, Mater. Des. 126 (2017) 268-277.

[46] A. Bahador, E. Hamzah, K. Kondoh, T.A. Abu Bakar, F. Yusof, H. Imai, S.N. Saud, M.K. Ibrahim, Mater. Des. 118 (2017) 152-162.

[47] P.S. Yu, M.G. Golkovski, I.A. Glukhov, A.Y. Eroshenko, V.A. Bataev, S.V. Fortuna, AIP Conf. Proc. 1698 (2016) 050004.

[48] L.-C. Zhang, H. Attar, Adv. Eng. Mater. 18 (2016) 463-475.

[49] C.S.S. de Oliveira, S. Griza, M.V. de Oliveira, A.A. Ribeiro, M.B. Leite, Powder Technol. 281 (2015) 91-98.

[50] K. Zhuravleva, M. Bönisch, K.G. Prashanth, U. Hempel, A. Helth, T. Gemming, M. Calin, S. Scudino, L. Schultz, J. Eckert, A. Gebert, Materials 6 (2013) 5700-5712.

[51] K. Zhuravleva, M. Bönisch, S. Scudino, M. Calin, L. Schultz, J. Eckert, A. Gebert, Powder Technol. 253 (2014) 166-171.

[52] I. Polozov, V. Sufiiarov, A. Popovich, D. Masaylo, A. Grigoriev, J. Alloys Compd. 763 (2018) 436-445.

[53] Y.-H. Hon, J.-Y. Wang, Y.-N. Pan, Mater. Trans. 44 (2003) 2384-2390.

[54] H.Y. Kim, S. Hashimoto, J.I. Kim, H. Hosoda, S. Miyazaki, Mater. Trans. 45 (2004) 2443-2448.

[55] C. Baker, Met. Sci. J. 5 (1971) 92-100.

[56] X.J. Wang, L.C. Zhang, M.H. Fang, T.B. Sercombe, Mater. Sci. Eng. A 597 (2014) 370-375.

[57] L. Thijs, F. Verhaeghe, T. Craeghs, J.V. Humbeeck, J.-P. Kruth, Acta Mater. 58 (2010) 3303-3312.

[58] C.L. Yang, Z.J. Zhang, S.J. Li, Y.J. Liu, T.B. Sercombe, W.T. Hou, P. Zhang, Y.K. Zhu, Y.L. Hao, Z.F. Zhang, R. Yang, Mater. Des. 157 (2018) 52-59.

[59] Y.J. Liu, S.J. Li, H.L. Wang, W.T. Hou, Y.L. Hao, R. Yang, T.B. Sercombe, L.C. Zhang, Acta Mater. 113 (2016) 56-67.

[60] D. Sun, D. Gu, K. Lin, J. Ma, W. Chen, J. Huang, X. Sun, M. Chu, Powder Technol. 342 (2019) 371-379.

[61] M. Guo, D. Gu, L. Xi, L. Du, H. Zhang, J. Zhang, Int. J. Refract. Met. Hard Mat. 79 (2019) 37-46.

[62] X.Z. Shi, S.Y. Ma, C.M. Liu, Q.R. Wu, Opt. Laser Technol. 90 (2017) 71-79.

[63] L.R. Sheppard, A.J. Atanacio, T. Bak, J. Nowotny, K.E. Prince, J. Phys. Chem. B 111 (2007) 8126-8130.

[64] A.E. Pontau, D. Lazarus, Phys. Rev. B 19 (1979) 4027-4037.

[65] A.R.G. Brown, D. Clark, J. Eastabrook, K.S. Jepson, Nature 201 (1964) 914-915.

[66] L. Wang, L. Xie, Y. Lv, L.-C. Zhang, L. Chen, Q. Meng, J. Qu, D. Zhang, W. Lu, Acta Mater. 131 (2017) 499-510.

[67] N. Otsu, IEEE Trans. Syst. Man Cybern. 9 (1979) 62-66.

[68] S.L. Sing, W.Y. Yeong, F.E. Wiria, J. Alloys Compd. 660 (2016) 461-470 .

[69] E.L. Pang, E.J. Pickering, S.I. Baik, D.N. Seidman, N.G. Jones, Acta Mater. 153 (2018) 62-70.

[70] Y. Al-Zain, H.Y. Kim, H. Hosoda, T.H. Nam, S. Miyazaki, Acta Mater. 58 (2010) 4212-4223.

[71] C.R.M. Afonso, G.T. Aleixo, A.J. Ramirez, R. Caram, Mater. Sci. Eng. C 27 (2007) 908-913.

[72] F. Sun, S. Nowak, T. Gloriant, P. Laheurte, A. Eberhardt, F. Prima, Scr. Mater. 63 (2010) 1053-1056.

[73] J. Su, Y. Li, M.-G. Duan, S. Liu, K. Liu, Mater. Sci. Eng. A 727 (2018) 29-37.

[74] U. Ramamurty, S. Jana, Y. Kawamura, K. Chattopadhyay, Acta Mater. 53 (2005) 705-717 .

[75] S.F. Jawed, C.D. Rabadia, Y.J. Liu, L.Q. Wang, Y.H. Li, X.H. Zhang, L.C. Zhang, J. Alloys Compd. 792 (2019) 684-693.

[76] P. Manda, U. Chakkingal, A.K. Singh, Mater. Charact. 96 (2014) 151-157.

[77] C.D. Rabadia, Y.J. Liu, G.H. Cao, Y.H. Li, C.W. Zhang, T.B. Sercombe, H. Sun, L.C. Zhang, Mater. Sci. Eng. A 732 (2018) 368-377.

[78] G. Wang, J. Yang, X. Jiao, Mater. Sci. Eng. A 654 (2016) 69-76.

[79] L. Zhou, T. Yuan, R. Li, J. Tang, M. Wang, F. Mei, J. Alloys Compd. 762 (2018) 289-300.

[80] C.D. Rabadia, Y.J. Liu, C.H. Zhao, J.C. Wang, S.F. Jawed, L.Q. Wang, L.Y. Chen, H. Sun, L.C. Zhang, Mater. Sci. Eng. A 766 (2019) 138340.

Table list:

Table 1 SLM manufacturing parameters used in this work and the corresponding relative densities measured by Archimedes method.

Parameters	Value	Value	Value	Value	Value
Laser power (W)	200	200	200	200	200
Laser scanning speed (mm/s)	500	625	750	1000	1250
Hatch space (μm)	100	100	100	100	100
Layer thickness (μm)	50	50	50	50	50
Energy density (J/mm^3)	80	64	53	40	32
Relative density (%)	99.0 ± 0.4	98.3 ± 0.4	98.1 ± 0.6	96.8 ± 1.4	96.2 ±1.1

Table 2 Comparison of mechanical properties of SLM-produced Ti-35Nb and other titanium alloys.

Material (wt%)	Process	Powder type	Micro structure	Vickers hardness (HV)	Test	Young's modulus (GPa)	Yield strength (MPa)	Ultimate strength (MPa)	Elong ation (%)	Ref.
Ti-35Nb	SLM	Tumbler mixed	Nb/α/α''/β	274 ± 7	Tensile	84 ± 2	648 ± 13	803 ± 33	3.9 ± 1.1	This work
Heat-treated Ti-35Nb (1000 °C)	SLM		Nb/α/α''/β	311 ± 16		86 ± 2	602 ± 14	713 ± 17	5.6 ± 1.9	This work
CP-Ti (Grade 2)	SLM	Prealloyed	α	213 ± 11	Tensile	112 ± 3	620 ± 20	703 ± 16	5.2 ± 0.3	[68]
Ti-35Nb	SLM	Tumbler mixed	Nb/α/β	240 ± 15	Compressive	84.7 ± 1.2	660 ± 13	-	38.5 ± 1.5	[12]
Annealed Ti-35Nb	SLM		Nb/α/β	252 ± 10		-	640 ± 12	-	47.3 ± 1.1	
Ti-16Nb	Sintering	Tumbler mixed	α/β	~340	-	~102	-	-	-	[14]
Ti-28Nb			α/β	~303	-	~100	-	-	-	
Ti-40Nb			α/β	~325	-	~105	-	-	-	
Ti-36.7Nb	Sintering	Ball milling	Nb/α/β	280	-	-	-	-	-	[46]
Ti-40Nb	SLM	Ball	α/α''/β	-	Compr	33 ± 2	-	968 ± 8	-	[50]

(porous)		milling			essive					
	Hot pressing	Ball milling	α/β/ω	-		77 ± 3	-	1400 ± 19	-	
Ti-25.5Nb	SLM	Ball milling	α'/β	312 ± 4	Tensile	-	501 ± 30	751 ± 14	-	[45]
Ti-39.3Nb			Nb/β	297 ± 3		-	516 ± 58	923 ± 38	-	
Ti-61.3Nb			Nb/β	356 ± 7		-	583 ± 67	1030 ± 40	-	
Ti-40.5Nb	SLM	Ball milling	Nb/α/β	266 ± 5	-	77 ± 0.4	-	-	-	[16]
Ti-40Nb	Sintering	Ball milling	α/β	-	-	-	-	-	-	[51]
Ti-45Nb		Milling prealloyed	β	-	-	-	-	-	-	
Ti-25Nb-22Al (annealed at 1350 °C)	SLM	Tumbler mixed	Nb/Al/α/O/α$_2$/B$_2$/β	-	Tensile	-	-	286	-	[52]
Ti-25Nb-22Al	Sintering	Ball milling	Nb/O/α$_2$/B$_2$/β	-	Tensile	-	353 - 586	464 - 690	2.6 - 5.0	[78]
Ti-45Nb	SLM	Prealloyed	β	~211	-	-	-	-	-	[17]
Ti-24Nb-4Zr-8Sn	SLM	Prealloyed	-	220 ± 6	Tensile	53 ± 1	563 ± 38	665 ± 18	13.8 ± 4.1	[41]
Ti-25Nb-3Zr-3Mo-2Sn	SLM	Prealloyed	β	202 -230	Tensile	-	592 ± 21	716 ± 14	37 ± 5.0	[26]
Ti-13Nb-13Zr	SLM	Prealloyed	α'/β	429 - 479	Tensile	65	794 ± 15	996 ± 13	5 ± 0.3	[79]

Figure list:
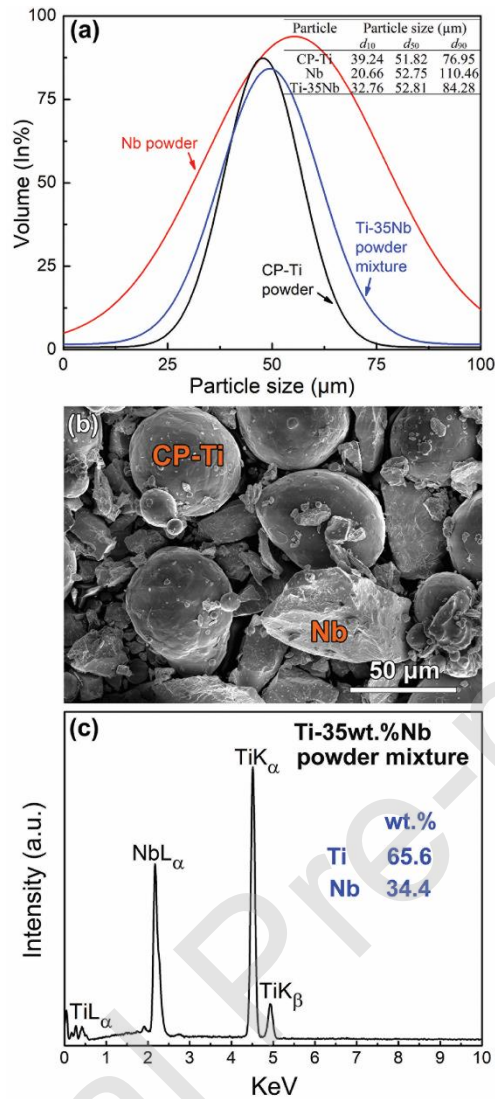
Fig. 1. (a) Powder particle size distribution of elemental powder mixture (Ti-35Nb), elemental Nb and CP-Ti powder, (b) morphology of the powder mixture, and (c) EDS analysis of the chemical composition for the powder mixture (Ti-35Nb).
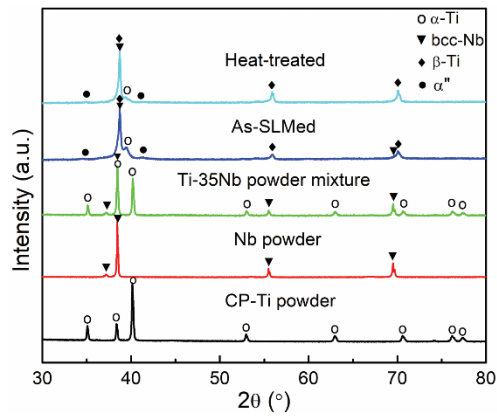
Fig. 2. XRD patterns of CP-Ti, Nb, powder mixture (Ti-35Nb), as-SLMed Ti-35Nb and heat-treated Ti-35Nb.
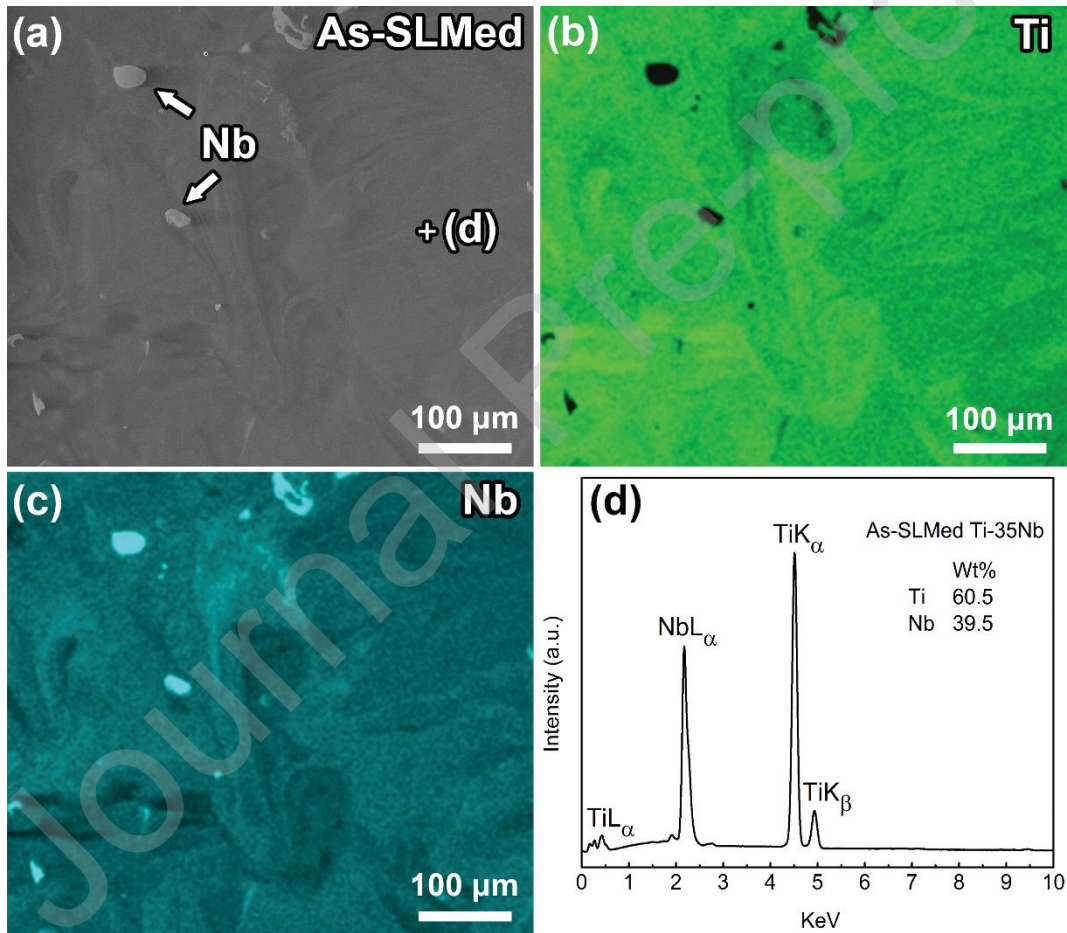

Fig. 3. (a) SEM microstructure image of as-SLMed Ti-35Nb composite and its EDS elemental mappings of (b) Ti and (c) Nb, (d) EDS spectrum for the location 'd' indicated in (a).
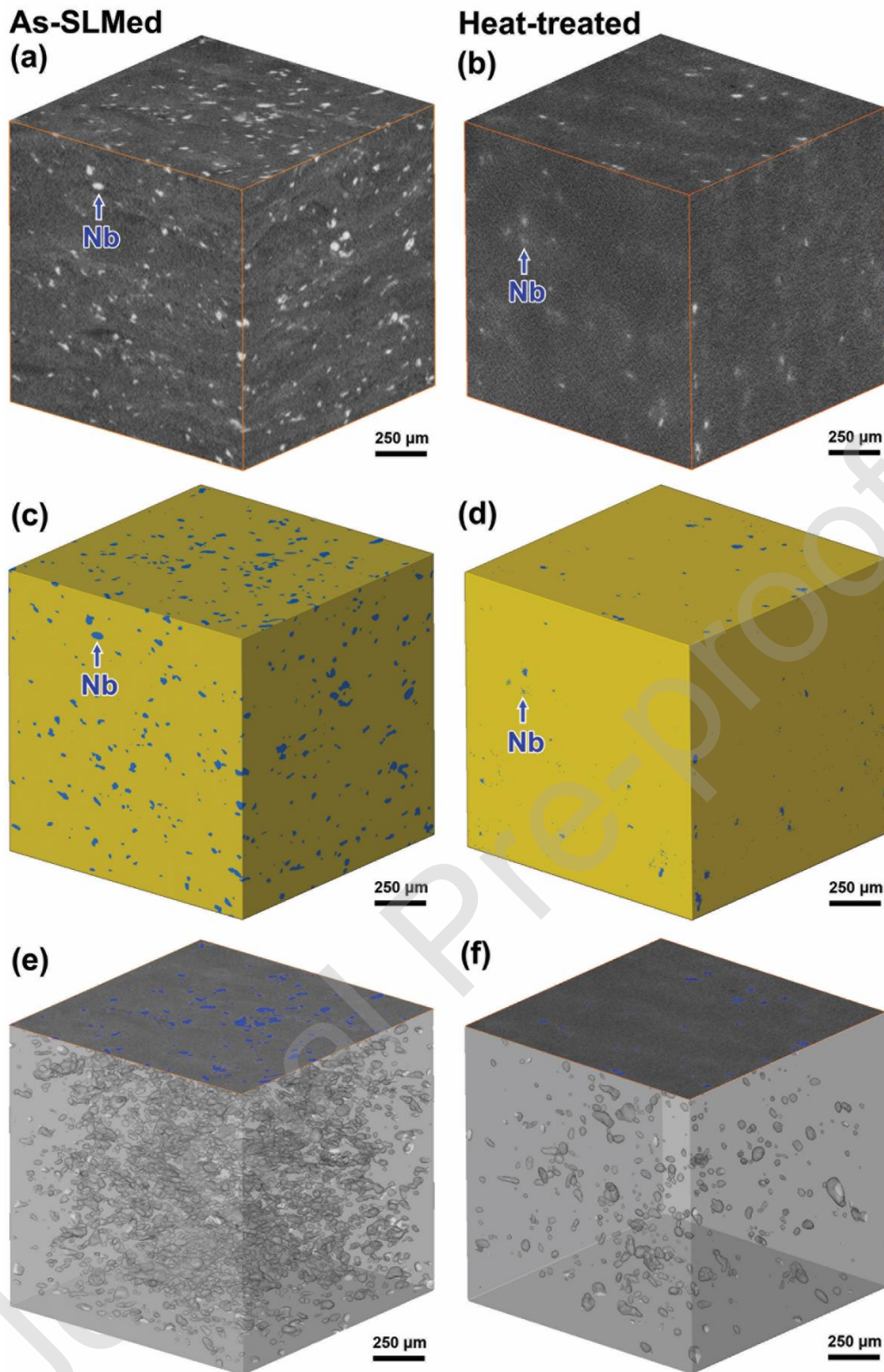
Fig. 4. The micro-CT 3D surface microstructures of (a) as-SLMed Ti-35Nb, and corresponding reconstructed images (c) and (e) the undissolved Nb particles, (b) heat-treated Ti-35Nb, and corresponding reconstructed images of (d) and (f) the undissolved Nb particles. (Heat treatment under Ar at 1000°C for 24h, and air cooled)
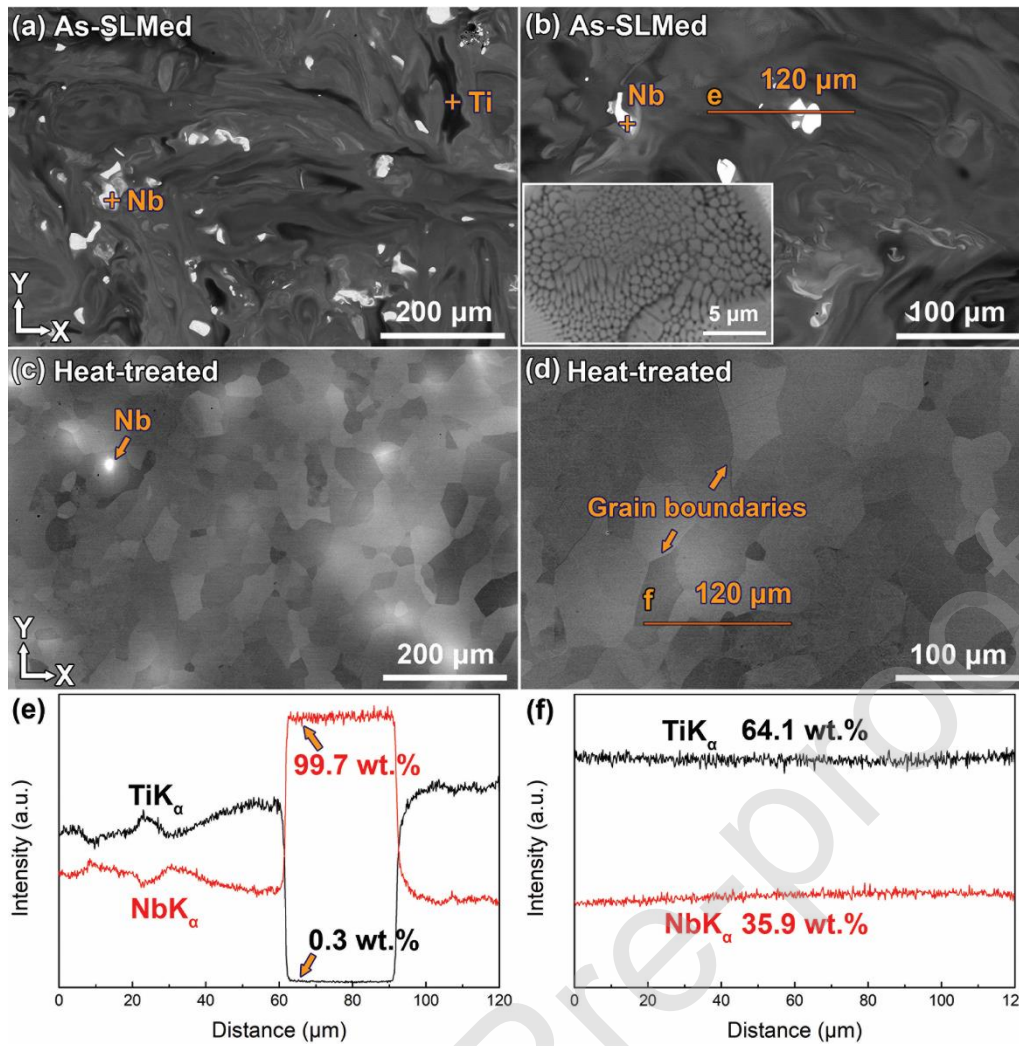
Fig. 5. Backscattered SEM images of Ti-35Nb (a)-(b) as-SLMed sample, and (c)-(d) heat-treated counterpart, (e)-(f) EDS line analyses for the lines indicated in (b) and (d) respectively. (Heat treatment under Ar at 1000°C for 24h, and air cooled)
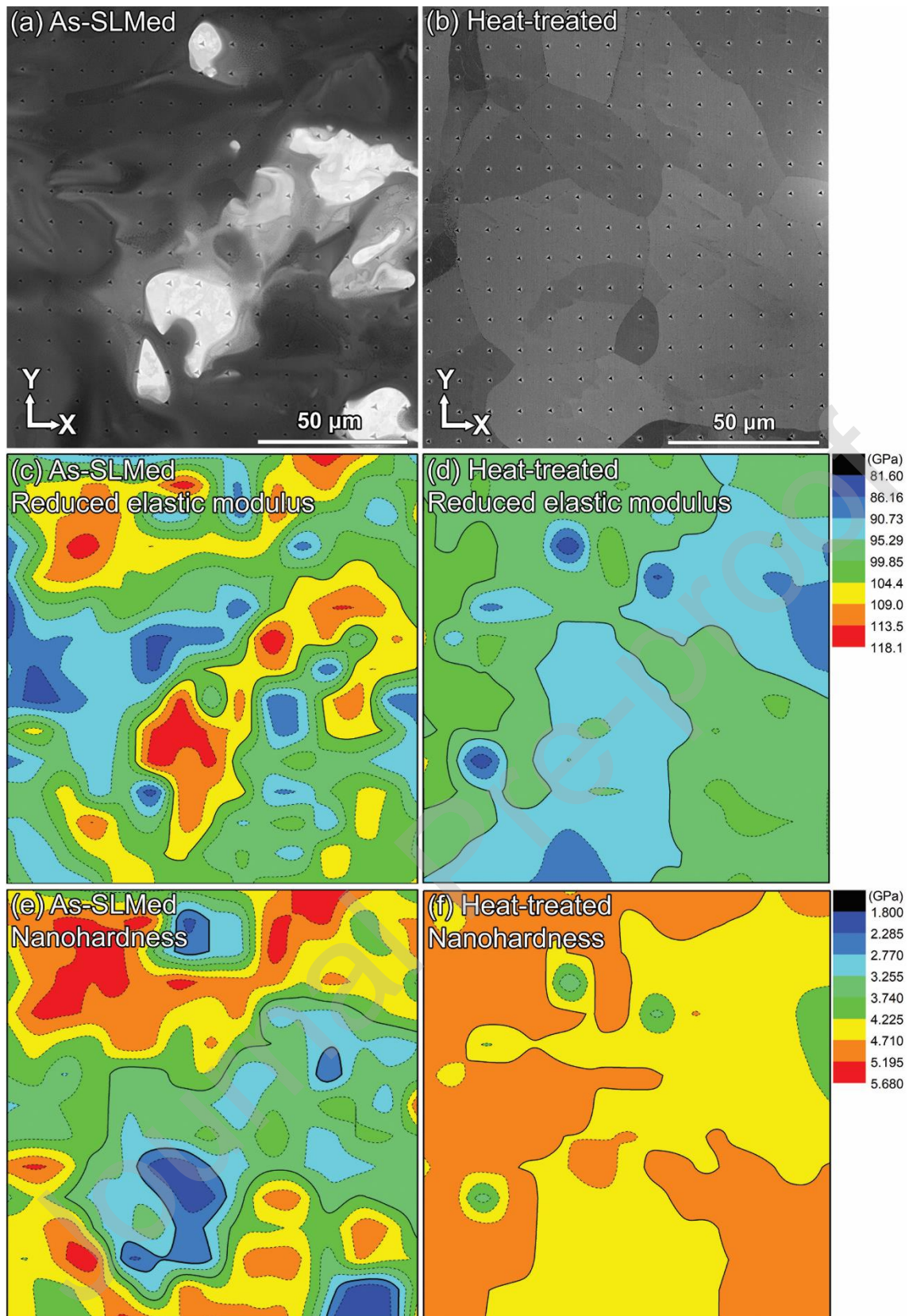
Fig. 6. (a) SEM image of the indentation spots for as-SLMed Ti-35Nb, and corresponding (c) reduced elastic modulus (E_r) mapping and (e) nano-hardness mapping; (b) SEM image of indentation spots for heat-treated Ti-35Nb, and corresponding (d) reduced elastic modulus (E_r) mapping and (f) nano-hardness mapping.

26
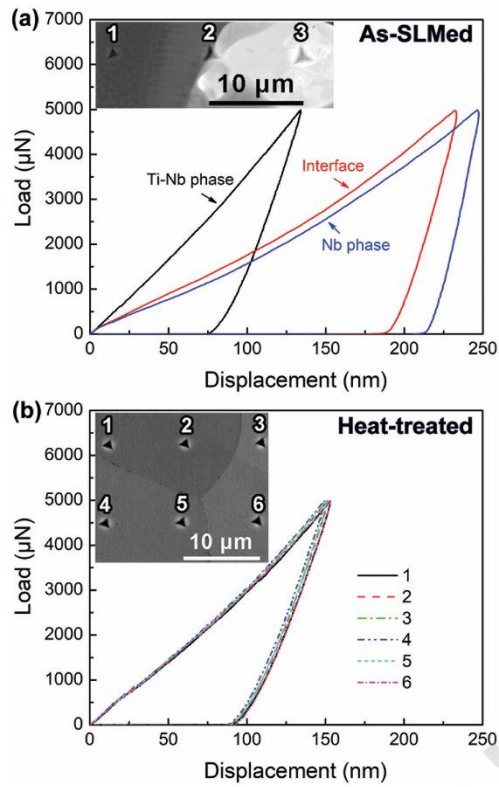
Fig. 7. Nanoindentation load-displacement curves of (a) as-SLMed Ti-35Nb and (b) heat-treated counterpart. The insets are SEM images show the individual indents.
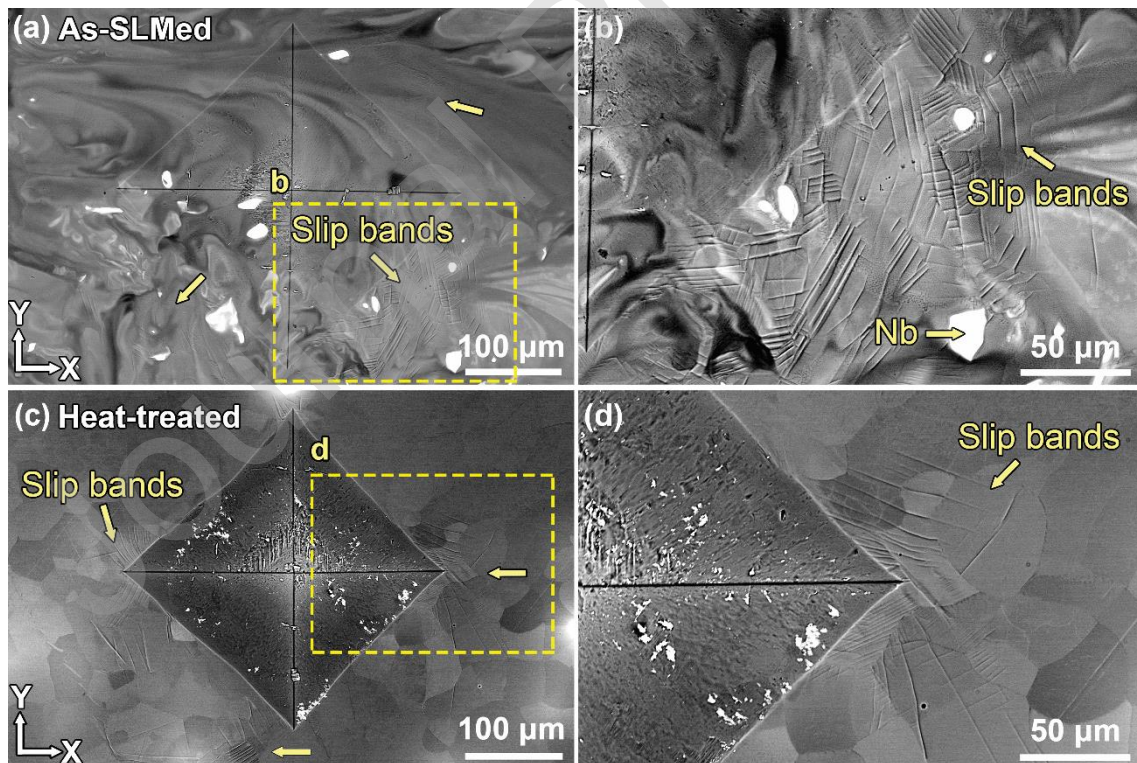
Fig. 8. Backscattered SEM images of an indent pattern (Vickers hardness) for (a)-(b) as-SLMed Ti-35Nb and (c)-(d) heat-treated counterpart. In (b) and (d), a magnified image from the dashed box in (a) and (c), respectively.
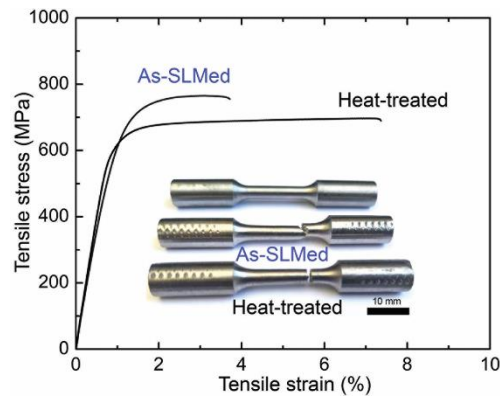
27

Fig. 9. The engineering tensile stress-strain curves for the as-SLMed Ti-35Nb samples and their heat-treated counterparts (inset is the fractured samples after tensile test).
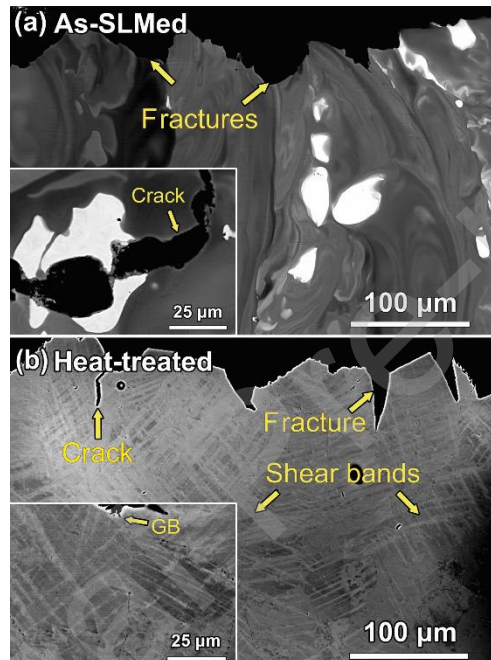

Fig. 10. Backscattered SEM deformation microstructures after tensile failure for (a) as-SLMed Ti-35Nb and (b) heat-treated counterpart. Insets are captured at high magnification.
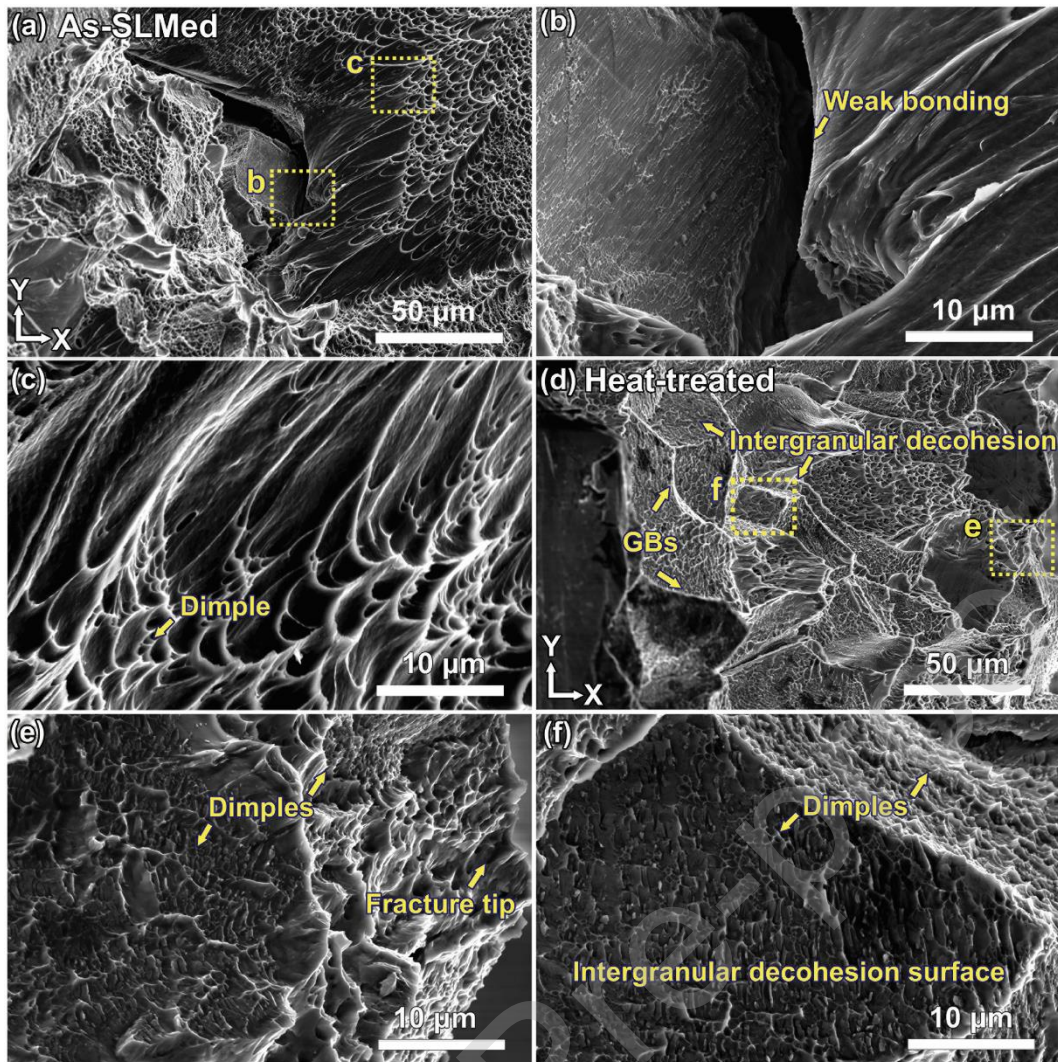
28

Fig. 11. Microstructure of fracture surfaces at the longitudinal section (side view from fracture) after tensile test: (a)-(c) as-SLMed Ti-35Nb sample, and (d)-(f) heat-treated counterpart.
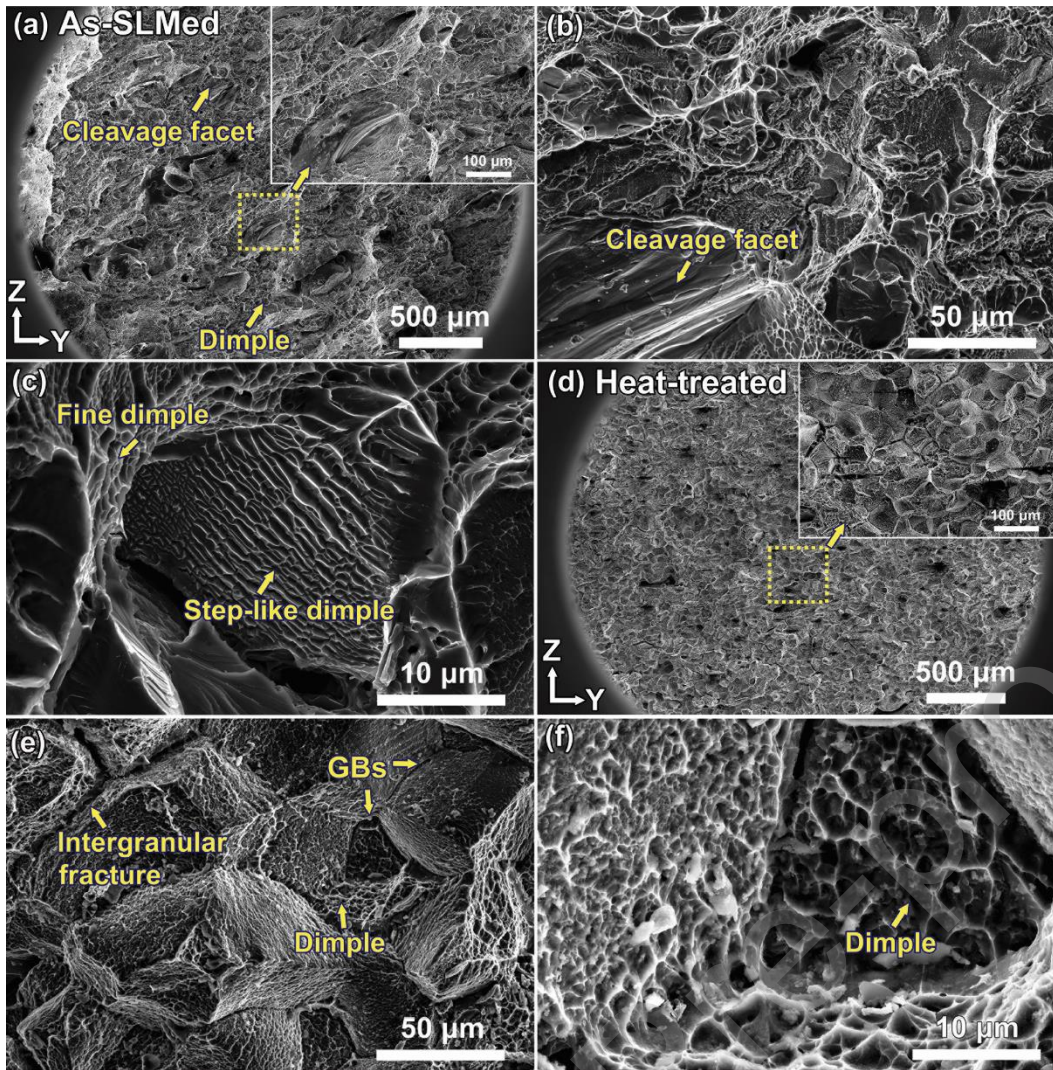
Fig. 12. Microstructure of fracture surfaces at the cross section (top view from fracture) after tensile failure: (a)-(c) as-SLMed Ti-35Nb sample, and (d)-(f) heat-treated counterpart.

30